JACS
JOURNAL OF THE AMERICAN CHEMICAL SOCIETY
pubs.acs.org/JACS
Article

Selective and Cooperative Photocycloadditions within Multistranded Aromatic Sheets

Bappaditya Gole, Brice Kauffmann, Arnaud Tron, Victor Maurizot, Nathan McClenaghan, Ivan Huc,* and Yann Ferrand*

Cite This: J. Am. Chem. Soc. 2022, 144, 6894–6906
Read Online
ACCESS | Metrics & More | Article Recommendations | Supporting Information

ABSTRACT: A series of aromatic helix-sheet-helix oligoamide foldamers composed of several different photosensitive diazaanthracene units have been designed and synthesized. Molecular objects up to 7 kDa were straightforwardly produced on a 100 mg scale. Nuclear magnetic resonance and crystallographic investigations revealed that helix-sheet-helix architectures can adopt one or two distinct conformations. Sequences composed of an even number of turn units were found to fold in a canonical symmetrical conformation with two helices of identical handedness stacked above and below the sheet segment. Sequences composed of an odd number of turns revealed a coexistence between a canonical fold with helices of opposite handedness and an alternate fold with a twist within the sheet and two helices of identical handedness. The proportions between these species could be manipulated, in some cases quantitatively, being dependent on solvent, temperature, and absolute control of helix handedness. Diazaanthracene units were shown to display distinct reactivity toward [4 + 4] photocycloadditions according to the substituent in position 9. Their organization within the sequences was programmed to allow photoreactions to take place in a specific order. Reaction pathways and kinetics were deciphered and product characterized, demonstrating the possibility to orchestrate successive photoreactions so as to avoid orphan units or to deliberately produce orphan units at precise locations. Strong cooperative effects were observed in which the photoreaction rate was influenced by the presence (or absence) of photoadducts in the structure. Multiple photoreactions within the aromatic sheet eventually lead to structure lengthening and stiffening, locking conformational equilibria. Photoproducts could be thermally reverted.

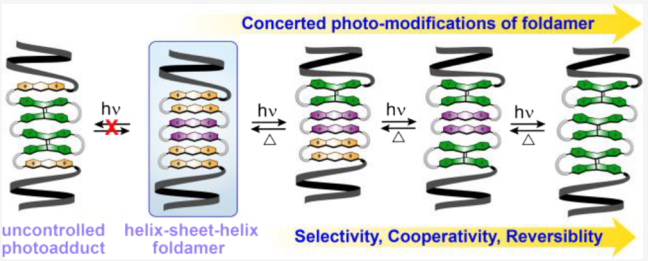

INTRODUCTION

Face-to-face $\pi-\pi$ stacking[1] promotes both defined molecular or supramolecular structures and specific electronic properties, in systems as diverse as nucleic acids,[2] organic reactions,[3] dye assemblies,[4] and solids for organic electronics.[5] Molecules or assemblies that possess a discrete number of stacked aromatic rings bear special interest because they provide an entry into the understanding and tailoring of their physical properties. Over the years, multiple strategies have been developed to control the well-ordered stacking of a defined number of aromatic rings, either all identical or different:[6] rigid polycyclophanes,[7] coordination cages,[8] and catenanes[9] represent conceptually distinct, yet successful approaches; flat, shape-persistent macrocycles may also be programmed to form finite aggregates with or without the assistance of a template;[10] rigid rods with hanging aromatic units may interdigitate to produce well-defined assemblies.[11] Compared to the approaches above, the folding of oligomers comprised of various aromatic monomers presents the advantage of unequivocal sequence control. Thus, aromatic foldamers, i.e., foldamers with aromatic rings in their main chain, have been designed to adopt well-defined multiturn helical conformations involving face-to-face stacking.[12] Foldamers containing strongly dipolar aromatics or alternating electron-rich and electron-poor aromatics may form pillar-like architectures driven by favorable interactions between stacked rings.[13] Aromatic foldamer sheets have also been designed using turns that promote face-to-face arrangements of adjacent units.[3b,14,15] Several reports have evidenced remarkable charge transport within discrete aromatic stacks, probably due to charge hopping between adjacent rings, i.e., not just through bonds but also through space.[16]

The examples cited above highlight that the control of stacked aromatic architectures is a well-developed area of research. Beyond the control of the structure lies the challenge of addressing these rings specifically so as to tune physical properties. As exemplified in rotaxanes[9b] and helical

Received: February 1, 2022
Published: April 5, 2022

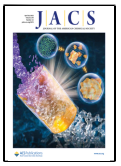

https://doi.org/10.1021/jacs.2c01269
J. Am. Chem. Soc. 2022, 144, 6894–6906

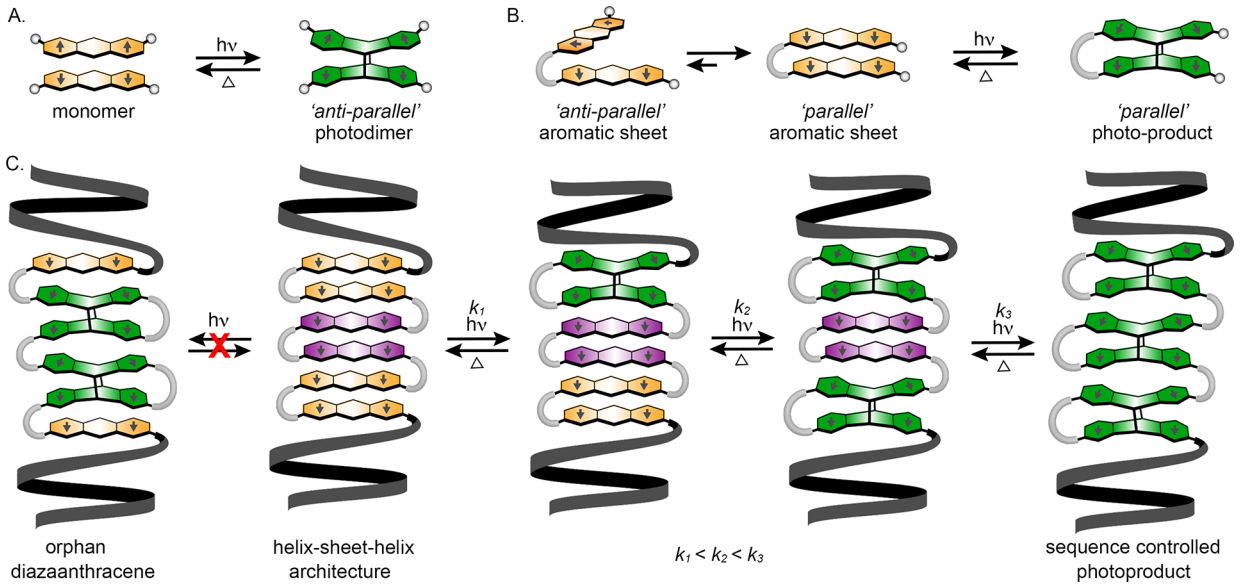

Figure 1. Schematic representation of (A) intermolecular and (B,C) intramolecular [4 + 4] 1,8-diazaanthracene photocycloadditions. Arrows shown in the aromatic rings represent local dipole orientations. (A) Intermolecular antiparallel photocycloaddition of diazaanthracenes directed by dipole moments. (B) Antiparallel and parallel arrangement of diazaanthracenes in an aromatic sheet. Photocycloaddition only occurs when the sheet is in its parallel configuration. (C) Cartoon representation of helix-multistranded sheet-helix architectures designed to undergo sequence specific intramolecular photocycloadditions. The photoproduct reverts to the starting material upon heating.

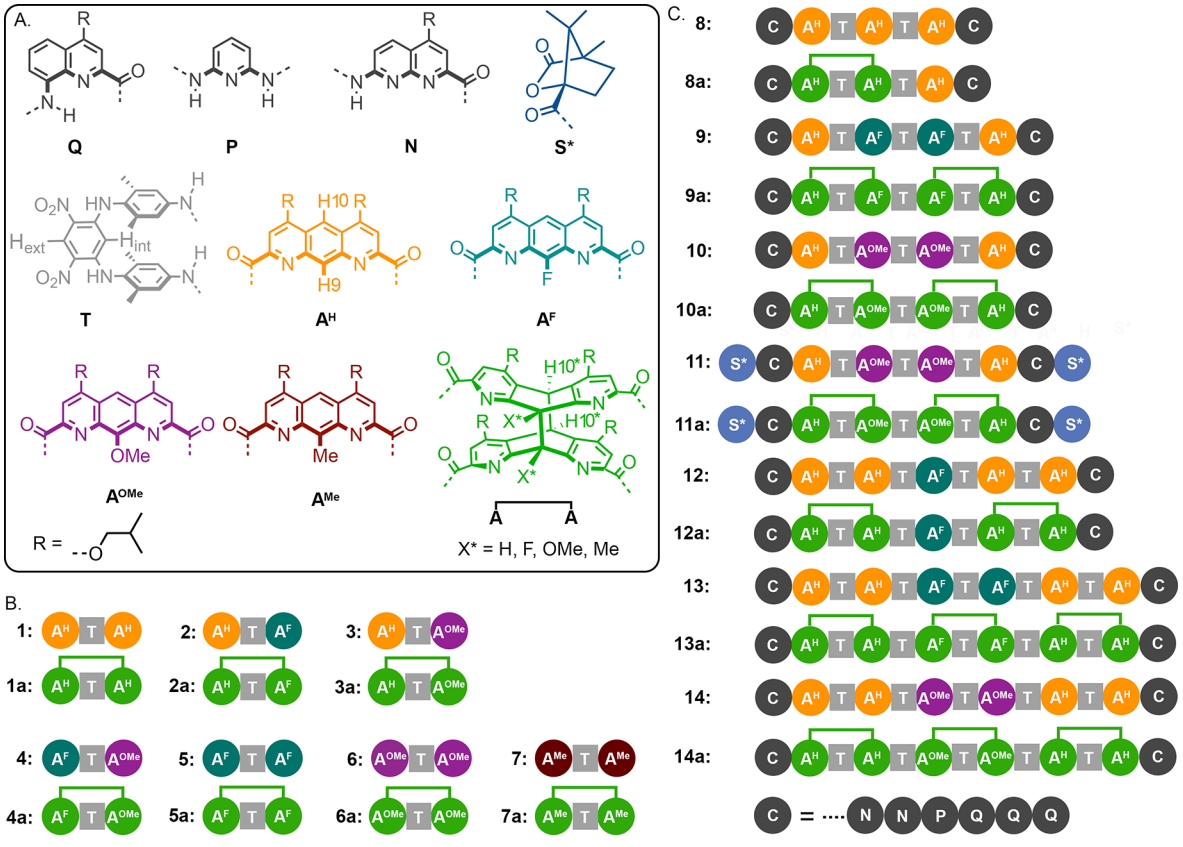

Figure 2. (A) Color-coded formula and corresponding abbreviations of amino acid, diamino, and diacid monomers. (B) Sequences **1**−**7** are aromatic sheets comprised of two diazaanthracene units having various groups in position 9, and **1a**−**7a** are their corresponding photocycloadducts. (C) **8**−**14** and **8a**−**14a** are helix-sheet-helix oligoamide sequences and their photoproducts, respectively. Terminal diazaanthracene and quinoline units bear a methyl ester group and an 8-nitro group (instead of an 8-amino function), respectively.

foldamers,[17] redox-responsive units allow for the injection or withdrawal of electrons, which eventually results in structural rearrangements. Photoresponsive monomers, typically azobenzenes or diarylethenes[18] and more rarely photocycloaddition precursors,[15e,19] have also been exploited to alter aromatic foldamer folding and their ability to bind to guest molecules.

https://doi.org/10.1021/jacs.2c01269
J. Am. Chem. Soc. 2022, 144, 6894−6906

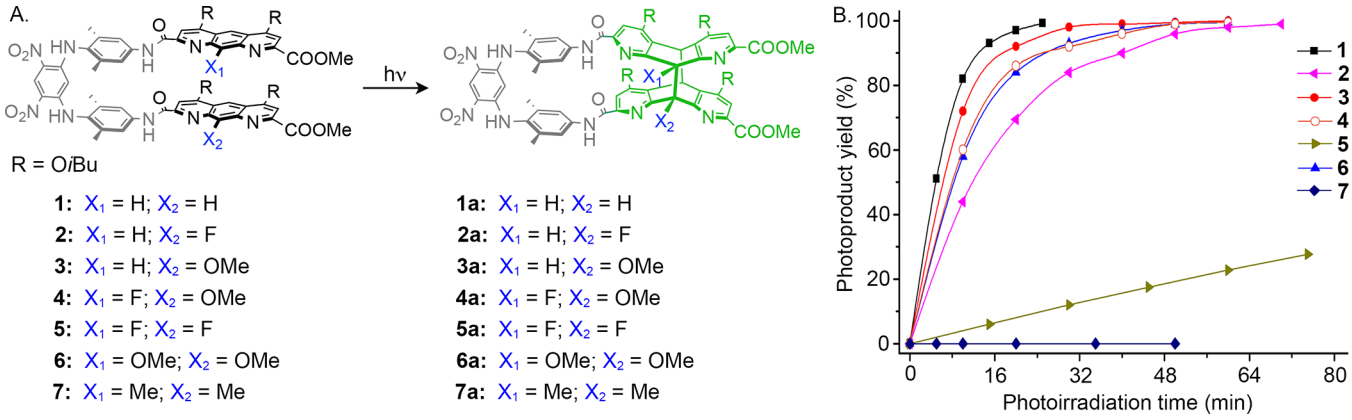

Figure 3. (A) Photocycloadduct formation from diazaanthracene sheets **1**−**7** (1 mM solution in $CDCl_3$) bearing varying substituents upon irradiation with λ = 320−390 nm under anaerobic conditions. (B) Time traces showing photocycloadduct yield as a function of photoirradiation time.

However, these systems often feature one photo- or electro-responsive aromatic unit or multiple copies of the same unit that all respond in the same manner and amplify the effect.

In contrast, we introduce herein the possibility to involve multiple photoresponsive units with distinct reactivity, thus allowing different photoreactions to take place in a certain order within a stack of aromatic rings produced by folding of an oligomer into a sheet structure. We use the classical photoinduced anthracene [4 + 4] cycloaddition reaction[20] to disrupt face-to-face stacking of anthracenes through the dearomatization of their central benzenic rings (Figure 1A,B). We demonstrate that photocycloaddition rates may be tuned by placing substituents in position 9 of the anthracene rings. Depending on the electronic and steric properties of the substituents, we show that it is possible to program photocycloadditions within a stack of anthracene rings in such a way that products having orphan anthracenes are avoided or, on the contrary, that products with orphan anthracenes at defined positions are generated (Figure 1C). The photoreactions eventually extend the sheet length and rigidify the overall architecture. We also present the unexpected discovery that photoreactions of anthracene units within a stack sometimes show positive cooperativity. In other words, the rate of a photoreaction may be influenced by the fact that another photoreaction has taken place or not.

RESULTS AND DISCUSSION

Tuning Photocycloaddition Kinetics in Model Systems. The reversible [4 + 4] cycloaddition leading to the dimerization of anthracene under photoirradiation is one of the most studied photochemical reactions[20] and has been extensively exploited in supramolecular systems.[21] In the case of substituted anthracenes, parallel and antiparallel (i.e., head-to-head and head-to-tail) isomeric photodimers may form. However, dipolar repulsions generally favor antiparallel isomers,[23] unless molecular or supramolecular constraints are imposed.[21,22] For example, 1,8-diazaanthracenes (i.e., pyrido[3,2-g]quinolines) undergo quantitative regioselective photodimerization in an antiparallel manner (Figure 1A) due to dipolar interactions between pyridine rings.[23c]

In the context of our studies on aromatic sheet foldamers,[15] we have introduced turn units, such as dinitro-diaminobenzene T (Figure 2A), that favor a parallel orientation of appended diazaanthracene units. In these systems, photocycloadditions were shown to yield the parallel photoproduct quantitatively (Figure 1B).[15e] This observation led us to consider the effect of substitutions at position 9 of the diazaanthracenes as a possible means to tune the efficiency of the [4 + 4] photocycloaddition. Herein, each diazaanthracene is noted A^X where X can be a hydrogen atom (H), a fluorine atom (F), a methyl (Me), or a methoxy (OMe) group in position 9 (Figure 2A). To assess the effect of the substituent in position 9, we prepared aromatic sheet models **1**−**7** (Figures 2B and 3A) comprised of two identical or different A^X units linked by a turn T (Schemes S1−S6). Synthetic procedures and characterization of all compounds are described in the Supporting Information (SI).

Each A^X-T-A^X sheet was irradiated in degassed $CHCl_3$ using UV light (λ = 320−390 nm) under anaerobic conditions using a 50 W portable mercury lamp. The occurrence of photocycloadditions was visible by the naked eye, the yellow color of the solutions becoming less intense (Figure S14). Reactions were monitored in parallel by proton nuclear magnetic resonance (^{1}H NMR) and electronic absorption spectroscopy. The latter methodology, utilizing monochromatic light (λ = 365 nm) and a chemical actinometer reference, afforded accurate photoreaction quantum yields (vide infra). Results from ^{1}H NMR monitoring are summarized in Figure 3B and show large variations of reaction rates depending on substituents. A^H-T-A^H sheet **1** reacted most efficiently (>82% completion after 10 min, Figure 3B) under the conditions used (Figure 2). The A^{OMe}-T-A^{OMe} sheet **6** was only slightly slower (>60% completion after 10 min). In contrast, the A^F-T-A^F sheet **5** underwent only 30% conversion after 75 min, and the A^{Me}-T-A^{Me} sheet **7** did not yield any traceable photoproduct. Nonetheless, all photocycloadditions, with the exception of A^{Me}-T-A^{Me},[24] were brought to completion and yielded a single photoproduct. Aromatic sheets composed of two different A^X moieties, for example, a slow and a fast reacting unit as in A^H-T-A^F, displayed intermediate reaction kinetics (Figure 3B).

In total, seven different aromatic sheets were prepared and each exhibited different rates of photocycloaddition. Electronic absorption spectroscopy corroborated these results (see the Supporting Information). The photocycloaddition quantum yields for all aromatic sheets ($\Phi_{photodimer}$) have been calculated, and the trends match well with the results of NMR spectroscopy studies (Table 1). In short, the results highlight that electronic factors and steric effects operate simultaneously

https://doi.org/10.1021/jacs.2c01269
J. Am. Chem. Soc. 2022, 144, 6894−6906

Table 1. Photoluminescence Quantum Yield (Φ_{Lum}) and Lifetime (τ) of Substituted Aromatic Sheets Are Given along with Their Corresponding Photoproduct Formation Quantum Yield ($\Phi_{photodimer}$)

oligomers	Φ_{Lum} [a]	τ [b] (ns)	$\Phi_{photodimer}$ [c]
1	2.0×10^{-3} (2.9×10^{-3})	<1	6.7×10^{-3}
2	0.1×10^{-3} (0.2×10^{-3})	<1	2.8×10^{-3}
3	4.5×10^{-3} (6.8×10^{-3})	<1	6.0×10^{-3}
4	6.1×10^{-3} (9.2×10^{-3})	<1	3.4×10^{-3}
5	0.4×10^{-3} (0.6×10^{-3})	<1	0.2×10^{-3}
6	5.3×10^{-3} (9.2×10^{-3})	<1	3.2×10^{-3}
7	1.6×10^{-3} (2.4×10^{-3})	<1	1.4×10^{-5}

[a]Optically dilute CH_2Cl_2 solution in aerobic and anaerobic (in parentheses) conditions. [b]Measured in anaerobic CH_2Cl_2. [c]Measured in $CHCl_3$ (30 μM) in anaerobic conditions.

and may act antagonistically on the photocycloaddition efficiency. Thus, an electron-donating group such as OMe promotes the [4 + 4] cycloaddition, whereas a bulky Me group induces an opposite effect due steric hindrance. As expected, the photoreaction is thermally reversible in 30 h at 333 K in $CHCl_3$ (Figures S2–S12). Attempts to revert the reaction using light irradiation at 254 nm were not successful.[25]

Helix-Sheet-Helix Design and Synthesis. Encouraged by these results, we surmised that appropriate combinations of A^X units in a multistranded aromatic oligoamide helix-sheet-helix sequence would potentially give rise to selective and sequential intramolecular photocycloadditions, via a precise control of the photoproduct formation efficiency. We previously studied the folding of bent aromatic sheets flanked by two helices.[15d,e] Here, we have extended this design so as to incorporate up to six stacked A^X units in the central sheet segment. In our earlier work, only up to three A^{Me} units, i.e., units unreactive under photoirradiation, had been incorporated. Sequences **8**–**14** (Figure 2C) were thus synthesized and characterized (see the Supporting Information). All comprise a central $A^x(TA^x)_n$ sheet ($2 \leq n \leq 5$) flanked with two terminal Q_3PN_2 helical segments. The helices have a conical shape because Q, P, and N monomers (in that order) code for an increasingly large helix diameter. These helical cones are abbreviated C in the sequences (Figure 2C).

To access a large number of sequences, we opted for a modular synthetic approach coupled with a convergent strategy. Practically, helical and sheet modules were prepared separately. For all the target sequences (**8**–**14**), we decided to use a unique hexameric helical segment Q_3PN_2 whose synthesis is fully mastered on the dozen gram scale.[15d] In parallel, the different dissymmetrical turn units A^XT were also prepared on gram scales. The helical segment was then elongated with one or two AT turns using PyBOP as a coupling agent to yield an intermediate helix-sheet segment. Finally, after a Boc deprotection of its amino function, the latter was coupled twice to either an anthracene A^X diacid or an A^X-T-A^X turn diacid to produce the desired helix-sheet-helix comprising 2, 3, 4, or 5 turn units (Schemes S8–S15). One should mention that the final couplings have not been optimized, yet the coupling reactions proved to be well behaved. The targeted large folded macromolecules (up to 7 kDa) could be obtained on scales larger than 100 mg quite straightforwardly.

Depending on the sequences, the nature of the A^X units involved was varied so that contiguous units in the stack may be identical or different. Thus, the rates of photocycloaddition with one neighbor or the other may vary as well. Based on prior knowledge,[15] we initially expected that $A^x(TA^x)_n$ sheets would place all A^X units in a parallel orientation. In the following, we show deviations from this pattern. Yet these deviations did not hamper the programming of pairwise photocycloadditions within large aromatic stacks. Nevertheless, before investigating photoreactions, we ascertained the conformations of these sequences.

Helix-Sheet-Helix Folds with Odd Numbers of A^X. Sequence **8**, integrating a central A^H-T-A^H-T-A^H segment, was first prepared, and its folding was evaluated in solution and in the solid state. In solution, ^{1}H NMR spectra in $CDCl_3$ revealed a single set of sharp and well spread resonances (Figures 4A and S15) indicative of folding into well-defined species. Chemical shift values were found to vary negligibly between 233 and 308 K (Figure S18). The number of amide resonances (eight) and the presence of a single H_{ext} signal (as defined in Figure 2A) indicated an overall symmetry of the molecule, which, considering its sequence, can only be C_2 symmetry. A

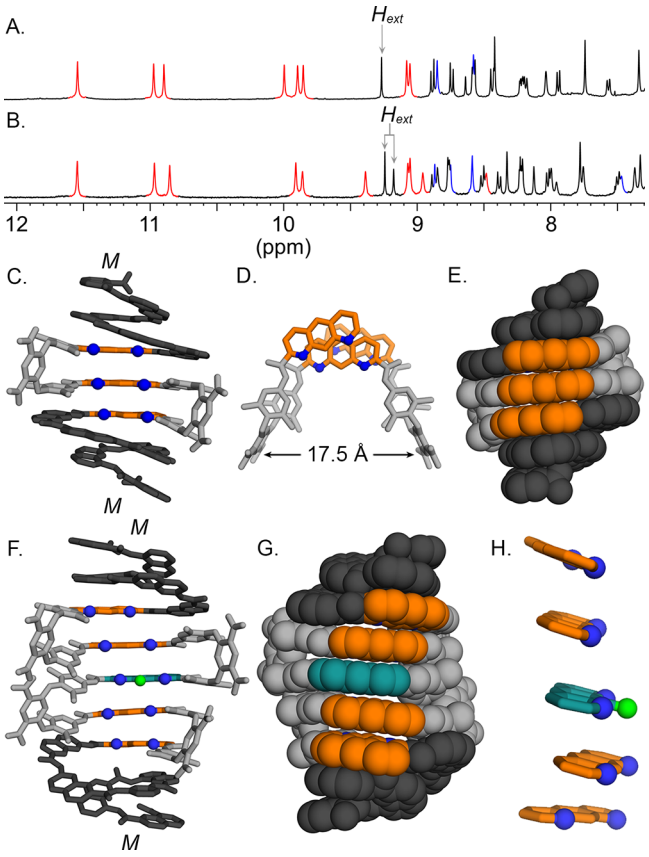

Figure 4. Part of the 400 MHz ^{1}H NMR spectra of (A) **8** and (B) **12** in 1 mM $CDCl_3$ solutions at 298 K. The amide and amine signals are highlighted in red and blue, respectively. (C–E) Views of the crystal structure of **8** shown in tube or space-filling representations. In (D), only the central sheet segment is shown; conical segments are omitted for clarity. (F) Front view of the energy-minimized molecular model of **12** using the Merck Molecular Force Field static (MMFFs) shown in tube representation. (G) Back view of the same in space-filling representation. (H) Parallel arrangement of the diazaanthracene in the model of **12**. The structures are shown with color-coded monomers as defined in Figure 2. Blue balls depict endocyclic nitrogen atoms. Hydrogen atoms, side chains, and solvent molecules are omitted for clarity.

https://doi.org/10.1021/jacs.2c01269
J. Am. Chem. Soc. 2022, 144, 6894–6906

crystal structure of **8** confirmed the symmetry and the predicted folding (Figure 4C−E). The three diazaanthracene rings stacked with their local dipoles parallel, and the two conical Q_3PN_2 segments have the same helix handedness. This helix-sheet-helix structure can be seen as a basket-like object with a central aperture of 17.5 Å. In this design, a photocycloaddition can only involve the central and one of the peripheral $\mathbf{A^H}$ units (see below).

Sequence **12**, an evolution of **8** with a five-anthracene stack, was then considered (Figure 2C). An odd number of anthracenes should preserve the C_2 symmetry and thus the same handedness of the two terminal helical segments. In contrast, an even number of anthracenes leads to plane-symmetrical objects and thus to a reversal of helical handedness. Unlike for **8**, growing single crystals of **12** was not successful. ^{1}H NMR in $CDCl_3$ and d_6-acetone showed one set of sharp resonances (Figures 4B and S19) and a global pattern that was very similar to that of **8**. Similarly, changing temperature from 238 to 318 K did not alter the spectrum (Figure S20). As for **8**, the number of amide signals (10) and the presence of two H_{ext} resonances, each integrating for two protons, was indicative of an average C_2 symmetry. Based on this information, an energy-minimized molecular model was built (Figure 4F−H). Within such an object, photocycloadditions may in principle yield diverse products. However, if the central A^F unit reacts slower than the two peripheral pairs of A^H units, then the latter would react first and a single product may be expected with an orphan central A^F unit.

Helix-Sheet-Helix Folds with Even Numbers of A^X. Stacks comprised of an even number of A^X units are attractive because, under ideal conditions, all A^X units may undergo an intramolecular photocycloaddition. Sequences **9** and **10** (each with four units) and **13** and **14** (each with six units) feature different combinations such that contiguous A^X units within the stack may be identical or different and thus potentially have different reactivity with their immediate neighbors. Unlike for sequences with an odd number of A^X units, the ^{1}H NMR spectra of **9** or **10** in $CDCl_3$ revealed not one but two sets of sharp resonances of different intensities, hinting at the presence of two conformations exchanging slowly on the NMR timescale (Figures 5 and S22). Each set of signals shows nine N*H* resonances, indicating that both species are symmetrical. In other solvents such as CD_2Cl_2, d_6-acetone, d_3-acetonitrile, and d_2-tetrachloroethane, noticeable variations of the proportion of the two species were observed (Figures S22 and S25). For example, the spectra of **9** showed one highly prevalent species (>95%, Figure S22) in d_3-acetonitrile and a 60/40 mixture in d_2-tetrachloroethane. The proportions between the species were found to also vary considerably with temperature: upon cooling a solution of **10** in $CDCl_3$ to 238 K, a unique conformation is stabilized (Figures 5A,B and S26). However, proportions did not change with concentration and DOSY experiments showed that they have the same hydrodynamic radius.

We first tried to predict the folding mode of sequences **9** and **10** using molecular modeling. The energy-minimized (MMFFs) canonical conformation of **10** is shown in Figure 5D,E. The model displays the expected stack of four parallel diazaanthracenes. The structure has an average plane of symmetry. Thus, the terminal helices possess opposite *P* and *M* handedness. This conformer was named **10**-*sym* (respectively **9**-*sym*) and is expected to be one of the two conformers observed in solution. Solid-state investigations shed light on

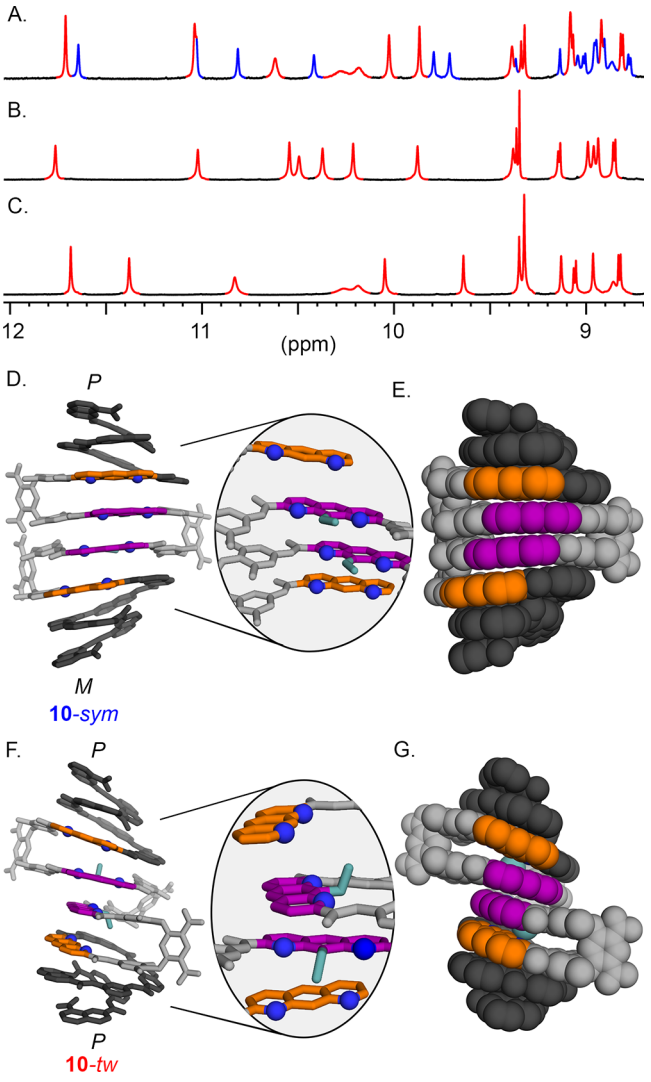

Figure 5. Part of the 700 MHz ^{1}H NMR spectra of **10** (1 mM) at (A) 298 K and (B) 238 K in $CDCl_3$. (C) Part of the 700 MHz ^{1}H NMR spectrum of **11** (1 mM) at 298 K in $CDCl_3$. Signals assigned to conformers **10**-*tw* and **10**-*sym* are highlighted in red and blue. (D,E) Views of an energy-minimized molecular model (MMFFs) of **10**-*sym* in tube and space-filling representations. The relative arrangement of diazaanthracene units is shown in the inset. (F,G) Views of the crystal structure of conformer **10**-*tw* in tube and CPK representations. The structures are shown with color-coded monomers as defined in Figure 2. Blue balls indicate endocyclic nitrogen atoms. Hydrogen atoms, side chains, and solvent molecules are omitted for clarity.

the other conformer. Single crystals of **10** were obtained from the slow diffusion of *n*-hexane into 1 mM $CHCl_3$ solution at 253 K, a temperature at which one of the two conformations is predominant. The solid-state structure revealed an unanticipated C_2-symmetrical conformation. Half of the foldamer had undergone a 180° rotation about a single aryl-amide bond between one xylyl group of the central T unit and its adjacent diazaanthracene unit (Figure 5F,G). Furthermore, the handedness of the corresponding helical segment had inverted. It follows that the central two A^{OMe} units are in an antiparallel arrangement, which gives the molecule a twisted shape. We termed this conformer **10**-*tw*. Antiparallel sheet conformations have been observed in other systems.[14g] Nevertheless, why they occur in **9** and **10** and also in **13** and **14** (see below) but not in **8** and **12** is unclear. The observation that the proportion

https://doi.org/10.1021/jacs.2c01269
J. Am. Chem. Soc. 2022, 144, 6894−6906

of **10**-*sym* compared to that of **10**-*tw* depends strongly on the temperature highlights a significant entropic contribution in this equilibrium, but its origin also remains unclear. Measuring an NMR spectrum immediately after dissolving a single crystal of **10**-*tw* did not allow us to assign this conformer to one set of signals or the other. Indeed, the spectrum already showed both sets of signals indicating that equilibrium had been quickly reached. Therefore, we prepared sequence **11** as a variant of **10** in which the helical segments are terminated by (1*S*)-(−)-camphanyl groups (**S*** in Figure 2). The effect of the **S*** groups is to quantitatively bias handedness toward *M* helicity.[26] It follows that the conformation of **11** should predominantly be **11**-*tw* because **11**-*sym* would require one *P* helix. As expected, the ^{1}H NMR spectrum of **11** shows only one set of signals (Figures 5C and S32) and this does not change with temperature (Figure S34). The spectrum of **11**-*tw* has analogies with the conformer of **10** that predominates at low temperatures. This, together with the fact that **10**-*tw* crystallized at low temperatures, suggests that **10**-*tw* is the conformer favored at low temperatures. The two conformers of **10** have thus been identified, and changing the temperature and solvent polarity provides conditions under which either the *tw* or the *sym* conformer prevails.

The folding of **13** and **14**, which possess a six-stranded sheet that combines A^{H} and A^{F}, or A^{H} and A^{OMe}, respectively, was investigated by ^{1}H and ^{19}F NMR. As for **9** and **10**, the spectra of **13** and **14** revealed two sets of resonances (Figures 6 and

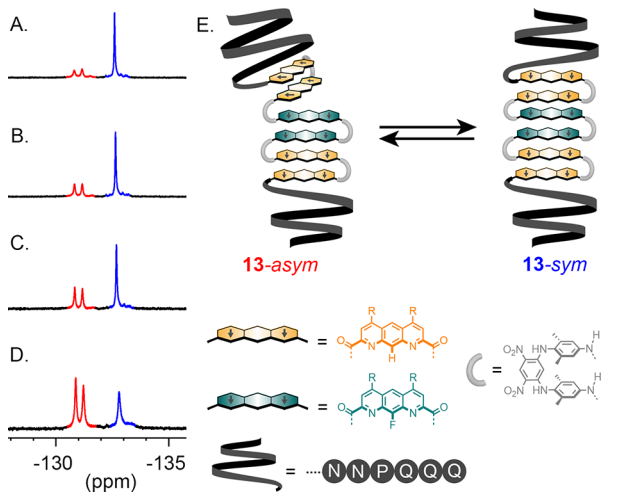

Figure 6. ^{19}F NMR spectra (376 MHz) of **13** (1 mM) at (A) 298 K; (B) 278 K; (C) 258 K; and (D) 248 K in d_6-acetone. Signals assigned to two conformers **13**-*sym* and **13**-*asym* are highlighted in blue and red, respectively. (E) Schematic representation of the dynamic exchange between the two conformers. Letter and color codes are defined in Figure 2.

S34 and S38), indicating the presence of two species under slow exchange on the NMR time scale. However, this time, the number of resonances shows that one species has an overall symmetry but not the other: ^{1}H-^{15}N HSQC spectra clearly show 11 N*H* resonances for one species and 22 for the other (Figures S36 and S39). Conversely, ^{19}F NMR spectra of **13**, which has two central A^{F} units, show a single fluorine resonance at −132.6 ppm for the symmetrical species and two resonances at −130.8 and −131.2 ppm for the dissymmetrical species (Figure 6A−D). The species were assigned to two conformers termed **13**-*sym* and **13**-*asym* and **14**-*sym* and **14**-*asym*. The proportions between the *sym* and *asym* conformers were again shown to vary with the temperature and solvent (Figures 6 and S35 and S38) but not with concentration. For instance, as for **9** and **10**, **14**-*sym* was the prevalent species in d_3-acetonitrile (Figure S38), and *asym* conformers were favored at low temperatures (Figure 6D).

Solid-state investigations allowed us to decipher the folding modes of these large multistranded helix-sheet-helix architectures. X-ray quality single crystals of **13**-*sym* were obtained by the slow diffusion of *n*-hexane in $CHCl_3$ solution (Figure 7A−D). The structure was solved and revealed an approximately (albeit tilted) six-stranded aromatic sheet with all A^{X} units in a parallel arrangement. Thus, as for **10**-*sym* (Figure 5D,E), the two terminal C segments have opposite helix handedness. Differences between the two structures are minor. The resulting overall shape is that of a 3 nm long and almost 2 nm wide basket, with all the X group of the A^{X} units lining the bottom of the cavity. An energy-minimized molecular model of **14**-*sym* based on the canonical structure of **13**-*sym* was calculated and is shown in Figure S62.

The structure of **14**-*asym* was also confirmed from crystals obtained by slow evaporation of an acetone solution (Figure 7E−H). The structure revealed the flip of a large part of the molecule due to the presence of one pair of antiparallel A^{X} units. This motif is similar to that observed in the structure of **10**-*tw* (Figure 5F,G). However, unlike in **10**-*tw*, it does not occur in the middle of the sequence between two A^{OMe} units but side-wise between an A^{H} and an A^{OMe}. We inferred that **13**-*asym* has a similar conformation to **14**-*asym*. NMR spectra unambiguously showed that the twist occurs at a single site and occurs only once. Yet, in the structures of **13** and **14**, multiple possibilities exist for such twists to occur at other sites or to occur more than once. The reasons why this is not the case are not clear. Spontaneous desymmetrization is not a common phenomenon. Clearly, the conformation of one part of the molecule must influence the conformation of the other part despite the large distances involved.

In summary, the in-depth conformational analysis of the new helix-sheet-helix foldamers allowed us to decipher their folding behavior. When the sheet contains an odd number of strands, only canonical folding is observed. If this number is even, then we observed two and only two conformers: one canonical and the other having one pair of antiparallel A^{X} units.

Cooperative Photocycloadditions within Multistranded Helix-Sheet-Helix Architectures. Motivated by the efficient conversion of aromatic sheet models **1**−**6** to their respective photoproducts **1a**−**6a**, photoirradiations were performed on longer sequences following similar protocols. All photoirradiation experiments were carried out in NMR tubes using millimolar solutions of oligomers in different solvents under anaerobic conditions (see the Supporting Information). First, we tested the photoirradiation of oligomers with three (**8**) or five (**12**) A^{X} units. We have shown above that these exist as a unique basket-like conformer in which all A^{X} are stacked parallel to one another. Oligomer **8** possesses three A^{H} units and may thus undergo one photocycloaddition. Upon irradiation, a 95% conversion to photoproduct **8a** after 90 min was observed by ^{1}H NMR (Figure S41). This reaction results in a loss of the initial C_2 symmetry and in the doubling of the number of proton resonances. The parallel configuration of the photoproduct was ascertained by characteristic resonances in the ^{1}H NMR spectrum: (i) a broad resonance at 4.67 ppm corresponding to

https://doi.org/10.1021/jacs.2c01269
J. Am. Chem. Soc. 2022, 144, 6894−6906

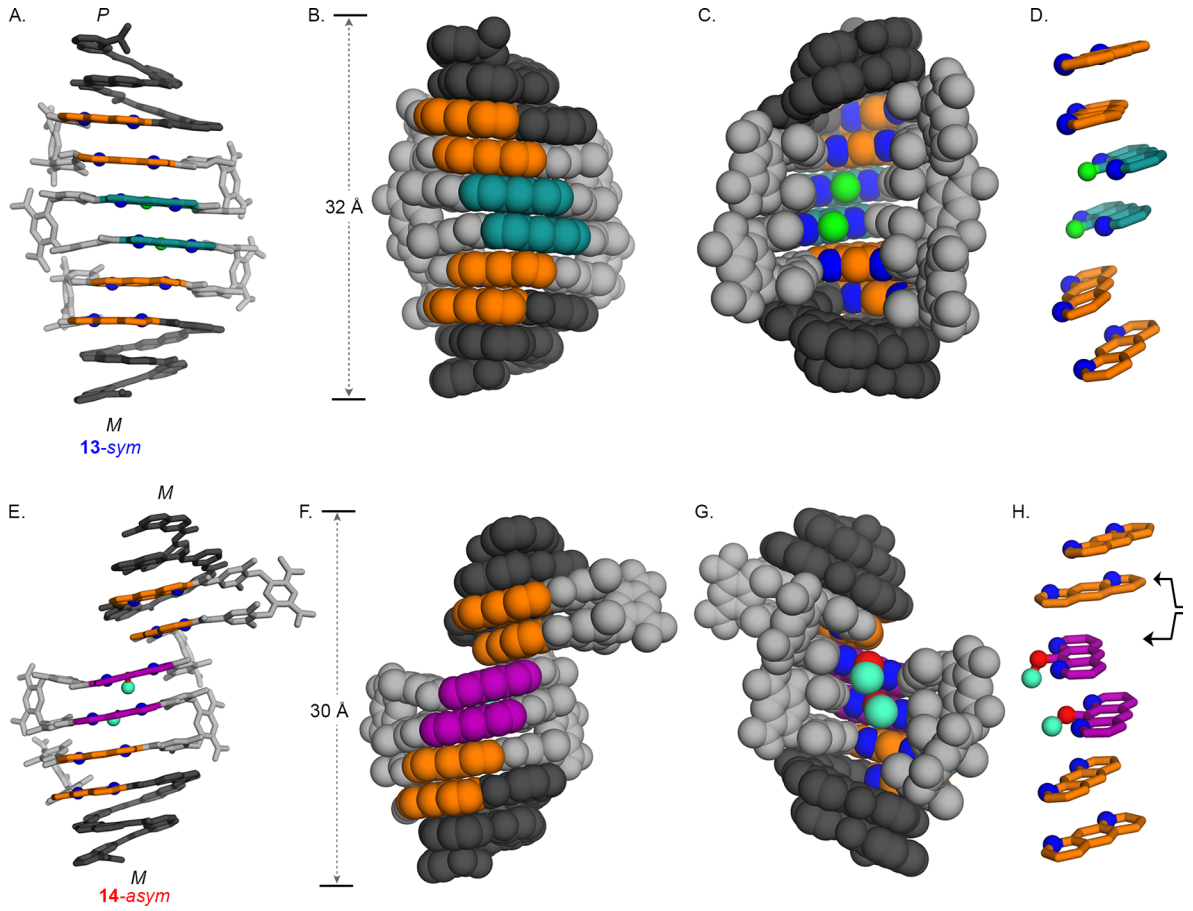

Figure 7. (A,B) Back views of the solid-state structure of **13**-*sym* in tube and space-filling representations, respectively. (C) Front view of **13**-*sym* in space-filling representation revealing the large cavity of the basket-like foldamer. (D) Orientation of the diazaanthracene units in **13**-*sym*. (E,F) Back views of the solid-state structure of **14**-*asym* in tube and space-filling representations, respectively. (G) Front view of **14**-*asym* in space-filling representation. (H) Orientation of the diazaanthracene units in **14**-*asym*. Arrows indicate the only pair of antiparallel diazaanthracene units. Color coding of monomers is defined in Figure 2. Blue balls indicate endocyclic nitrogen atoms. Hydrogen atoms, side chains, and solvent molecules are omitted for clarity.

the two H10* protons (as defined in Figure 2) and (ii) two doublets at 5.03 and 5.17 ppm assigned to the coupled nonequivalent H9* protons. An energy-minimized structure was obtained using MMFFs, highlighting that a canonical folding is preserved in spite of the butterfly-like shape of the photoadduct (Figure S60). We also note that the photoreaction of **8** is somewhat slower than that of simple sheet **1**. This trend was general for all sequences and hints at a photoshielding effect of the helical cones that flank the central sheet. The reverse reaction to **8** was achieved quantitatively by heating a solution of **8a** at 333 K for 36 h (Figure S42).

Sequence **12** possesses five A^X units and may in principle yield multiple photoproducts. However, the presence of the central A^F and the faster photoreaction of A^H units hinted at the possible selective pairwise reaction of the latter, leaving an orphan A^F in the middle of a unique symmetrical photoproduct. This, however, proved not to be straightforward. Irradiating **12** for 5 h in $CDCl_3$ or in d_6-acetone resulted in the emergence of more than one species with unresolved (i.e., broad) ^1H NMR signals (Figure S54). ^{19}F NMR spectra suggest a two-step process: a first mono-photocycloaddition after 1 h followed, after 5 h of irradiation, by a second photocycloaddition (Figure S55). Because all other photoreactions could be monitored and the products identified thanks to sharp NMR spectra and because the discrimination between A^H/A^H and A^H/A^F pairs was evidenced in other sequences, the investigation of **12** was not pursued further. We instead focused on multistranded oligomers with an even number of A^X units. Due to their bimodal folding modes, we anticipated more complex analysis, but, on the contrary, experiments instead showed remarkably selective conversions.

Sequences **9** and **10** were designed with four-stranded sheets so that the central pair of $\mathbf{A}^X$ units reacts slower than the peripheral pairs. As depicted in Figure 8A, the photocycloaddition of the two central A^F units of **9**-*sym* would produce two orphan peripheral A^H units. However, we have seen above (Figure 3B) that the photocycloaddition of an A^F/A^F pair is much slower than that of A^F/A^H. The difference is lesser in the case of the A^{OMe}/A^{OMe} and A^{OMe}/A^H pairs found in compound **10**, and selectivity may be more difficult to achieve in this case. Photoirradiation was carried out on both **9** and **10** in d_6-acetone and monitored by ^1H and ^{19}F NMR. Photoconversion was essentially complete after 5 and 1 h, respectively. The overall reaction rates thus reflect well the higher photoreactivity of A^{OMe} than A^F. The final spectra revealed the presence of two products and showed no orphan A^H unit (Figures 8 and S42 and S45). Thus, selective cycloadditions are achieved in both cases; even A^{OMe} and A^H react preferentially. In the case of **9**, proof that the products consist of photocycloadditions between A^H and A^F units came from

https://doi.org/10.1021/jacs.2c01269
J. Am. Chem. Soc. 2022, 144, 6894−6906

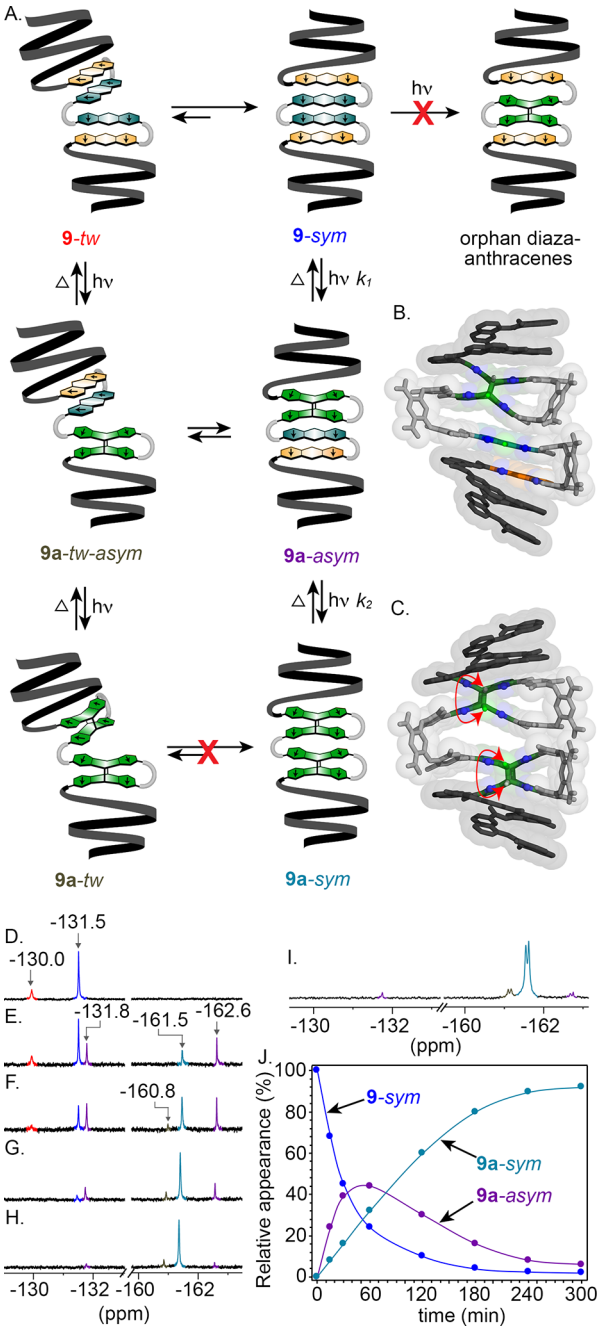

Figure 8. (A) Schematic illustration of stepwise photoadduct formation of **9**. Initially two conformers, **9**-*tw* and **9**-*sym*, are at equilibrium at room temperature. Both may undergo stepwise photoreactions giving final products **9a**-*tw* and **9a**-*sym*, respectively. Photoreaction between the two central A^F units is much slower. (B,C) Energy-minimized molecular models (MMFFs) of **9a**-*asym* and **9a**-*sym* in tube representation. Monomers are color-coded as in Figure 2. Blue balls indicate endocyclic nitrogen atoms. Hydrogen atoms and side chains are not shown for clarity. Red double headed arrows indicate scalar coupling between F9* and H9* as reflected in (I) 376 MHz $^{19}F\{^1H\}$ NMR spectra of **9** (1 mM in d_6-acetone) at 298 K after (D) 0 min; (E) 30 min; (F) 1 h; (G) 2 h; and (H) 5 h of photoirradiation. (I) ^{19}F NMR (not decoupled) spectrum after 5 h irradiation. Signals assigned to individual species are highlighted with colors as in (A). (j) Plot showing the time course of the proportions of **9**-*sym*, **9a**-*sym*, and **9a**-*asym* during the reaction. The usual color code is maintained throughout.

the observation of doublets in proton-coupled ^{19}F NMR (Figure 8J). These doublets originate from the scalar coupling between the H9* and the F9* atoms in the cyclo-addition products (Figure 8C, see Figure 2A for the definition of H9* and F9*).

The photoreaction of **9** in d_6-acetone could be monitored in detail by both $^{19}F\{^1H\}$ (i.e., proton decoupled, Figure 8D−H) and ^1H NMR (Figure S43). After 30 min of photoirradiation of the initial **9**-*sym*/**9**-*tw* mixture (3:1 ratio), two new species emerged (Figure 8E). One species shows a single ^{19}F resonance at −161.5 ppm and proved to be a final product. The other displays two ^{19}F resonances at −131.8 and −162.6 ppm. It is thus dissymmetrical, and it disappears, after reaching a maximum, as the reaction continues (Figure 8J). At the end of the reaction, two products have appeared (at −161.5 and −160.8 ppm), and traces of the intermediate remain (Figure 8H). These two products can reasonably be assigned to **9a**-*sym* and **9a**-*tw* and the intermediate to **9a**-*asym*. Nonlinear fitting of the observed ^1H NMR resonance intensity change of each species during the photoreaction, considering two sequential photodimerization reactions, yielded apparent kinetic constants $k_1 = 4.4 \times 10^{-4}$ s^{-1} and $k_2 = 2.0 \times 10^{-4}$ s^{-1} (Figure 8A). While the magnitude of these observed values depends on the irradiation conditions, the ratio of these values, k_1/k_2, corresponds to the relative efficiency of the photodimerization reactions. When taking into account the changing absorption/removal of one of two pairs of reactive anthracenes accompanying the initial photodimerization reaction, within experimental error, the second photodimerization reaction is seen to proceed similarly and is thus unimpeded by the first. As anticipated, **9a**-*tw* and **9a**-*sym* (as well as **10a**-*tw* and **10a**-*sym*) do not interconvert upon changing the temperature (Figure S48) or solvent (Figure S49). Therefore, photocycloadditions have locked the respective conformers and prevent exchanges.

The complete absence of orphan units in the photoproducts is remarkable in the case of **10** because the rates of photocycloadditions within A^H-T-A^H (**1**), A^H-T-A^{OMe} (**3**), and A^{OMe}-T-A^{OMe} (**6**) do not differ to a great extent (Figure 3). One may comment that the existence of *tw* conformers should favor this outcome, but the abundance of a **10a**-*sym* suggests that other effects are at play and that the reaction selectivity is further enhanced in the multistranded sheets.

Remarkably, the final **9a**-*sym*/**9a**-*tw* ratio (10:1) differs from the initial **9**-*sym*/**9**-*tw* ratio. Photoirradiation of compound **10** in d_6-acetone also led to a **10a**-*sym*/**10a**-*tw* ratio significantly larger than the initial **10**-*sym*/**10**-*tw* ratio (Figure S47). In contrast, when photoirradiation was performed in $CDCl_3$, the initial **10**-*sym*/**10**-*tw* ratio (1:2) was reflected in the proportion of products (Figure S46). A plausible mechanism for the stepwise photocycloaddition is presented in Figure 8A, and models are shown in Figures 8B,C and S64. The prevalence of product **9a**-*sym* can be interpreted in several ways. For example, if intermediate **9a**-*tw*-*asym* is less stable than intermediate **9a**-*asym*, a conformational rearrangement may occur between the two before **9a**-*tw*-*asym* is converted in the final **9a**-*tw*. Another reason may be that **9**-*sym* undergoes a first photocycloaddition much faster than **9**-*tw*. Both hypotheses would explain that the **9a**-*tw*-*asym* intermediate remained below detection levels.

Complementary information came from the photoreaction of chiral sequence **11**, which, as we have seen, exists as an exclusive **11**-*tw* conformer. This compound undergoes a clean conversion to a single photoproduct, **11a**-*tw* (Figure S51).

https://doi.org/10.1021/jacs.2c01269
J. Am. Chem. Soc. 2022, 144, 6894−6906

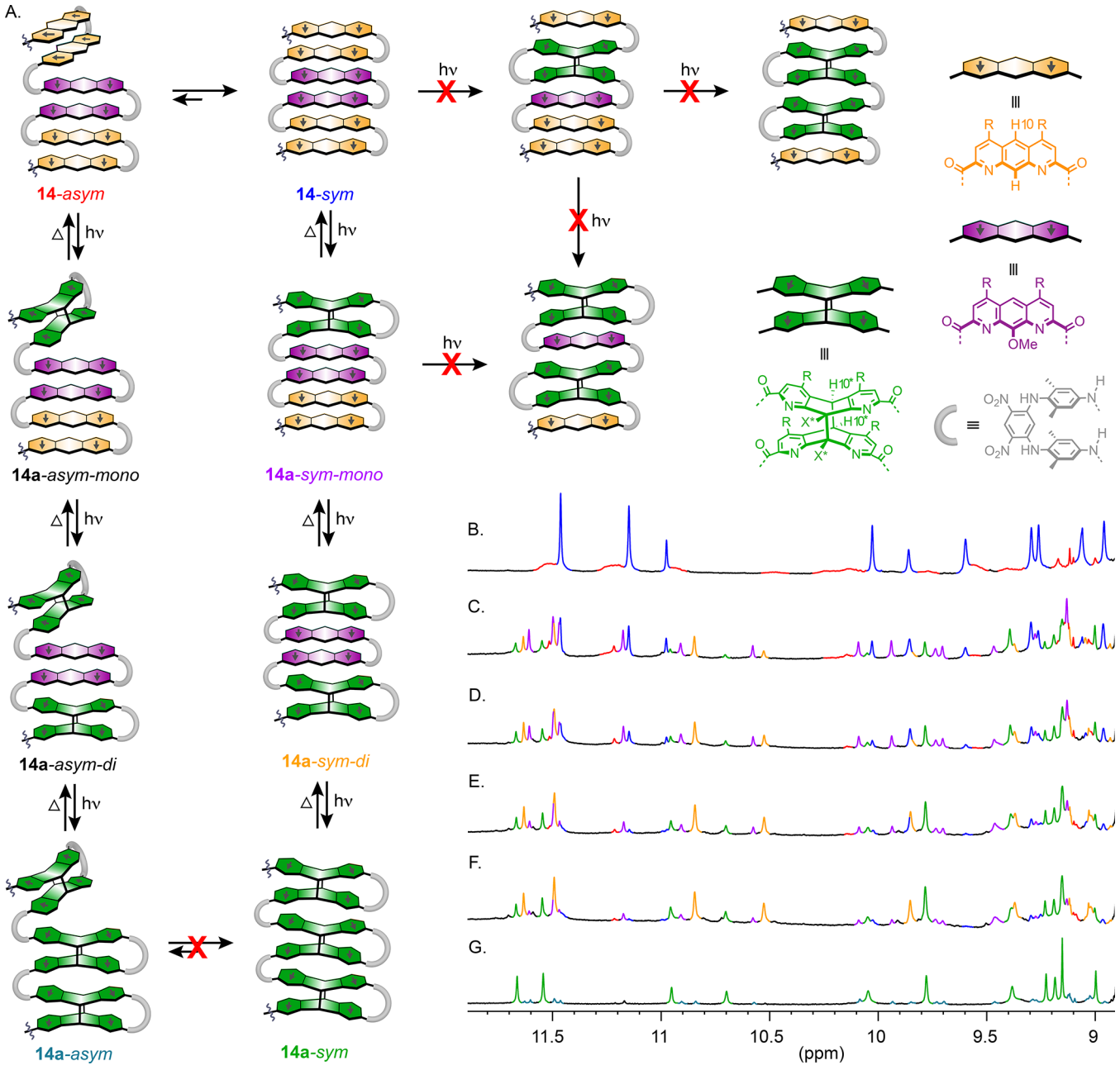

Figure 9. (A) Schematic illustration of stepwise photoreactions of **14**. Initially two conformers, **14**-*asym* and **14**-*sym*, are in equilibrium at room temperature. Both may undergo stepwise photoreactions to produce **14a**-*asym* and **14a**-*sym*, respectively. Pathways that would yield orphan A^X units were not observed. Terminal helices have been omitted for clarity. Part of the 700 MHz ^{1}H NMR spectra of **14** (1 mM in d_6-acetone) at 298 K under photoirradiation after (B) 0 h; (C) 2 h; (D) 3 h; (E) 5 h; (F) 7 h; and (G) 10 h after isolation of the products by precipitation. Signals assigned to individual species (**14a**-*sym*, **14a**-*asym*, **14a**-*sym-mono*, **14a**-*sym-di*, **14a**-*asym*, and **14a**-*sym*) are highlighted with color as depicted in (A).

Remarkably, this conversion occurs without any detectable **11a**-*tw-asym* intermediate, indicating a very strong cooperativity: the photoreaction of **11**-*tw* must be much slower than that of **11a**-*tw-asym*, which does not accumulate. These results are in agreement with the hypothesis that the initial *tw* species are the least reactive of all and reveal an intriguing interplay between conformations and successive photoreactions that results in remarkable selectivity. Additionally, it is worth noting that eight stereogenic centers are generated simply by irradiating the sequence with light. Indeed, a careful examination of the NMR spectrum of **11a** (Figure S53) revealed the existence of a single set of amide resonances, which indicates a full control of the stereogenicity of the eight new asymmetric centers. The outcome of this photoreaction is that folding combined with camphanyl moieties that are positioned several angstroms away from diazaanthracenes can fully control the stereoselectivity of the photoreaction.

Finally, we demonstrated the orchestration of three consecutive photocycloadditions within 7 kDa helix-sheet-helix foldamers **13** and **14**. In both compounds, sheet segments are composed of two peripheral pairs of A^H units and a central pair of A^F or A^{OMe} units. Based on the results shown in Figure 3, we envisaged that the pairs of A^H monomers would photoreact first followed by the pairs of A^F or A^{OMe} units while anticipating that reaction completion may be hard to reach with a pair of A^F units. Such a pathway would exclude orphan

https://doi.org/10.1021/jacs.2c01269
J. Am. Chem. Soc. 2022, 144, 6894−6906

A^X units in the final products. Since **13** and **14** each exist as two *asym* and *sym* conformers (Figures 6 and 7), different intermediates and two final products can be envisaged (Figure 9A).

Photoirradiation of **13** was first monitored in d_6-acetone by ^{1}H- and ^{19}F NMR. Despite the presence of two initial *asym* and *sym* conformers, ^{19}F{^{1}H} NMR spectroscopy clearly showed the formation of a single dissymmetrical intermediate followed by a single symmetrical product (Figure S56). The absence of ^{19}F signals near −162 ppm indicated that none of these species resulted from a cycloaddition of an A^F unit, which have thus remained intact. The intermediate was therefore assigned to **13a**-*sym-mono* and the final product to **13a**-*sym-di*. In summary, selective photoreaction of A^H units was achieved, *asym* photoproducts were not observed, and no orphan A^X units were produced, but the pair of A^F units did not react after 12 h.

In the case of **14** (Figure 9B−G), two main intermediates, one dissymmetrical and one symmetrical, were observed as well as a main photoproduct, which were assigned to **14a**-*sym-mono*, **14a**-*sym-di*, and **14a**-*sym*, respectively (Figure 9A). ^{1}H NMR confirmed that all A^X units of **14a**-*sym* could react, including the central pair of A^{OMe}, and that no orphan $\mathbf{A}^X$ unit was formed. Isolation of the final product by slow precipitation in acetone revealed that it contains a small amount (∼15%) of dissymmetrical species that we interpreted as being **14a**-*asym*. Intermediates toward that species were not seen because their proportion remained minor throughout the reaction. Changing the solvent or temperature did not alter the **14a**-*sym*/**14a**-*asym* ratio, confirming that the structures are locked by intramolecular cycloadditions (Figures S56 and S57). Molecular models of **14a**-*sym* revealed that the three intramolecular cycloadditions resulted in an extension of molecular length of 0.8 nm compared to **14**-*sym* (3.9 vs 3.1 nm) (Figure S67).

CONCLUSIONS

In summary, we have designed and synthesized high molecular weight abiotic helix-sheet-helix architectures comprised of multiple functional diazaanthracene units that can be selectively modified upon light irradiation. The modular and oligomeric nature of the helix-sheet-helix backbones allowed us to access straightforwardly to seven different sequences using convergent synthetic schemes. Both the number of aromatic turns and the nature of the photoreactive units may be conveniently varied. We first deciphered the folding behavior of these macromolecules and found that folding depends on the number of turn units. An even number of aromatic turns systemically led to unique folded species with a canonical sheet folding and two helices of identical handedness. In contrast, an odd number of turn units led to an equilibrium between a symmetrical canonical sheet and a dissymmetrical twisted sheet whose proportions were found to vary significantly with the solvent and temperature. This equilibrium may in principle be quantitatively shifted favoring one or the other species by controlling the handedness of the terminal helical segments—canonical species have helices of opposite handedness, and twisted species have helices of opposite handedness—though this was implemented only in the case of one dissymmetrical species.

We also found that the photoreactivity of the diazaanthracene monomers was finely tunable upon introducing various substituents in position 9. We thus introduced different diazaanthracene units at the defined position of the helix-sheet-helix sequences to implement multiple selective [4 + 4] photocycloadditions and trigger photomodifications of the aromatic backbones at precise locations, avoiding orphan units or, on the contrary, programming the formation of orphan units. Monitoring the photoreactions revealed that they were not only influenced by the nature of the diazaanthracene substituents. The canonical (symmetrical) or twisted (dissymmetrical) conformation of the foldamer also influences reaction rates as well as the presence or not of an intermediate photoadduct in the structure. In some cases, this led to strongly cooperative photoreactions in which the fully photoreacted product was generated without any detectable amounts of partly reacted intermediates. Up to three distinct photocycloadditions were implemented in the same helix-turn-helix architecture leading to the stiffening of the backbone and to a length extension of the sheet segment. This lengthening of the sheet is reminiscent of previous work on helix extension by the groups of Aida[17a] and of Yashima.[27] The predictability of the folding of the aromatic helix-sheet-helix structures and the fine tuning of the photoreactions may find applications in photocontrolled guest release, or for the photocontrol of charge transport properties through selective disruption of face-to-face π-π stacking interactions.[16e,f] Efforts toward these objectives are currently in progress in our laboratories and will be reported in due course.

ASSOCIATED CONTENT

Supporting Information

The Supporting Information is available free of charge at https://pubs.acs.org/doi/10.1021/jacs.2c01269.

Details on the synthesis and structural characterizations of compounds, NMR spectra, UV−vis spectra, and crystallographic and molecular mechanics data including Schemes S1−S15, Figures S1−S67, and Tables S1−S4 (PDF)

Accession Codes

CCDC 2144662−2144663 and 2144666−2144667 contain the supplementary crystallographic data for this paper. These data can be obtained free of charge via www.ccdc.cam.ac.uk/data_request/cif, or by emailing data_request@ccdc.cam.ac.uk, or by contacting The Cambridge Crystallographic Data Centre, 12 Union Road, Cambridge CB2 1EZ, UK; fax: +44 1223 336033.

AUTHOR INFORMATION

Corresponding Authors

Ivan Huc − *Department of Pharmacy, Ludwig-Maximilians-University, 81377 Munich, Germany; Cluster of Excellence e-Conversion, 85748 Garching, Germany;* orcid.org/0000-0001-7036-9696; Email: ivan.huc@cup.lmu.de

Yann Ferrand − *Univ. Bordeaux, CNRS, Bordeaux Institut National Polytechnique, CBMN (UMR 5248), 33600 Pessac, France;* orcid.org/0000-0002-6552-6914; Email: yann.ferrand@u-bordeaux.fr

Authors

Bappaditya Gole − *Univ. Bordeaux, CNRS, Bordeaux Institut National Polytechnique, CBMN (UMR 5248), 33600 Pessac, France;* Present Address: Department of Chemistry, School of Natural Sciences, Shiv Nadar

https://doi.org/10.1021/jacs.2c01269
J. Am. Chem. Soc. 2022, 144, 6894−6906

University, Gautam Buddha Nagar, Uttar Pradesh 201314, India; orcid.org/0000-0002-0001-6569
Brice Kauffmann − *Univ. Bordeaux, CNRS, INSERM, Institut Européen de Chimie Biologie (UMS3033/US001), 33600 Pessac, France;* orcid.org/0000-0002-2932-3255
Arnaud Tron − *Univ. Bordeaux, CNRS, Institut des Sciences Moléculaires (UMR5255), 33405 Talence cedex, France*
Victor Maurizot − *Univ. Bordeaux, CNRS, Bordeaux Institut National Polytechnique, CBMN (UMR 5248), 33600 Pessac, France;* orcid.org/0000-0001-6104-796X
Nathan McClenaghan − *Univ. Bordeaux, CNRS, Institut des Sciences Moléculaires (UMR5255), 33405 Talence cedex, France;* orcid.org/0000-0003-0285-1741

Complete contact information is available at: https://pubs.acs.org/10.1021/jacs.2c01269

Author Contributions

The manuscript was written through contributions of all authors. All authors have given approval to the final version of the manuscript.

Notes

The authors declare no competing financial interest.

■ ACKNOWLEDGMENTS

This work was supported by the post doc program of the Excellence Initiative of Bordeaux University (B.G.) and the France−Germany International Research Project "Foldamers Structures and Functions" (IRP FoldSFun). This work has benefited from the facilities and expertise of the Biophysical and Structural Chemistry platform (BPCS) at IECB, CNRS UMS3033, Inserm US001, and Bordeaux University.

■ REFERENCES

(1) Martinez, C. R.; Iverson, B. L. Rethinking the term "pi-stacking.". *Chem. Sci.* **2012**, *3*, 2191.
(2) (a) Giese, B. Long-distance electron transfer through DNA. *Annu. Rev. Biochem.* **2002**, *71*, 51. (b) Genereux, J. C.; Barton, J. K. Mechanisms for DNA charge transport. *Chem. Rev.* **2010**, *110*, 1642. (c) Sontz, P. A.; Muren, N. B.; Barton, J. K. DNA charge transport for sensing and signaling. *Acc. Chem. Res.* **2012**, *45*, 1792. (d) Arnold, A. R.; Grodick, M. A.; Barton, J. K. DNA charge transport: from chemical principles to the cell. *Cell Chem. Biol.* **2016**, *23*, 183.
(3) (a) Krenske, E. H.; Houk, K. N. Aromatic interactions as control elements in stereoselective organic reactions. *Acc. Chem. Res.* **2013**, *46*, 979. (b) Bornhof, A.-B.; Bauzá, A.; Aster, A.; Pupier, M.; Frontera, A.; Vauthey, E.; Sakai, N.; Matile, S. Synergistic anion−$(\pi)_n$−π catalysis on π-Stacked foldamers. *J. Am. Chem. Soc.* **2018**, *140*, 4884. (c) Kürti, L.; Blewett, M. M.; Corey, E. J. Origin of enantioselectivity in the Jacobsen epoxidation of olefins. *Org. Lett.* **2009**, *11*, 4592. (d) Corey, E. J.; Noe, M. C. A Rational approach to catalytic enantioselective enolate alkylation using a structurally rigidified and defined chiral quaternary ammonium salt under phase transfer conditions. *J. Am. Chem. Soc.* **1996**, *118*, 11038. (e) Anderson, C. D.; Dudding, T.; Gordillo, R.; Houk, K. N. Origin of enantioselection in hetero-Diels−Alder reactions catalyzed by naphthyl-TADDOL. *Org. Lett.* **2008**, *10*, 2749.
(4) (a) Würthner, F.; Saha-Möller, C. R.; Fimmel, B.; Ogi, S.; Leowanawat, P.; Schmidt, D. Perylene bisimide dye assemblies as archetype functional supramolecular materials. *Chem. Rev.* **2016**, *116*, 962. (b) Kim, T.; Kang, S.; Kirchner, E.; Bialas, D.; Kim, W.; Würthner, F.; Kim, D. Switching resonance character within merocyanine stacks and its impact on excited-state dynamics. *Chem* **2021**, *7*, 715. (c) Herbst, S.; Soberats, B.; Leowanawat, P.; Stolte, M.; Lehmann, M.; Würthner, F. Self-assembly of multi-stranded perylene dye J-aggregates in columnar liquid-crystalline phases. *Nat. Commun.* **2018**, *9*, 2646.
(5) (a) Pisula, W.; Feng, X.; Mullen, K. Charge-carrier transporting graphene-type molecules. *Chem. Mater.* **2011**, *23*, 554. (b) Yao, Z.-F.; Wang, J.-Y.; Pei, J. Control of π−π stacking via crystal engineering in organic conjugated small molecule crystals. *Cryst. Growth Des.* **2018**, *18*, 7. (c) Noveron, J. C.; Lah, M. S.; Del Sesto, R. E.; Arif, A. M.; Miller, J. S.; Stang, P. J. Engineering the structure and magnetic properties of crystalline solids via the metal-directed self-assembly of a versatile molecular building unit. *J. Am. Chem. Soc.* **2002**, *124*, 6613. (d) Sokolov, A. N.; Friscic, T.; Blais, S.; Ripmeester, J. A.; MacGillivray, L. R. Persistent one-dimensional face-to-face π-stacks within organic cocrystals. *Cryst. Growth Des.* **2006**, *6*, 2427.
(6) Klosterman, J. K.; Yamauchi, Y.; Fujita, M. Engineering discrete stacks of aromatic molecules. *Chem. Soc. Rev.* **2009**, *38*, 1714.
(7) (a) Breidenbach, S.; Ohren, S.; Vögtle, F. Nanometre-scale molecular ribbons. *Chem. − Eur. J.* **1996**, *2*, 832. (b) Shibahara, M.; Watanabe, M.; Iwanaga, T.; Matsumoto, T.; Ideta, K.; Shinmyozu, T. Synthesis, structure, and transannular π−π interaction of three- and four-layered [3.3]paracyclophanes. *J. Org. Chem.* **2008**, *73*, 4433.
(8) (a) Yamauchi, Y.; Yoshizawa, M.; Akita, M.; Fujita, M. Engineering double to quintuple stacks of a polarized aromatic in confined cavities. *J. Am. Chem. Soc.* **2010**, *132*, 960. (b) Ono, K.; Yoshizawa, M.; Akita, M.; Kato, T.; Tsunobuchi, Y.; Ohkoshi, S.-I.; Fujita, M. Spin crossover by encapsulation. *J. Am. Chem. Soc.* **2009**, *131*, 2782. (c) Engelhard, D. M.; Freye, S.; Grohe, K.; John, M.; Clever, G. H. NMR-based structure determination of an intertwined coordination cage resembling a double trefoil knot. *Angew. Chem., Int. Ed.* **2012**, *51*, 4747.
(9) (a) Ashton, P. R.; Goodnow, T. T.; Kaifer, A. E.; Reddington, M. V.; Slawin, A. M. Z.; Spencer, N.; Stoddart, J. F.; Vicent, C.; Williams, D. J. A [2] catenane made to order. *Angew. Chem., Int. Ed.* **1989**, *28*, 1396. (b) Asakawa, M.; Ashton, P. R.; Balzani, V.; Credi, A.; Hamers, C.; Mattersteig, G.; Montalti, M.; Shipway, A. N.; Spencer, N.; Stoddart, J. F.; Tolley, M. S.; Venturi, M.; White, A. J. P.; Williams, D. J. A chemically and electrochemically switchable [2]catenane incorporating a tetrathiafulvalene unit. *Angew. Chem., Int. Ed.* **1998**, *37*, 333. (c) Fujita, M.; Ibukuro, F.; Hagihara, H.; Ogura, K. Quantitative self-assembly of a [2]catenane from two preformed molecular rings. *Nature* **1994**, *367*, 720.
(10) (a) Shua, L.; Mayor, M. Shape-persistent macrocycle with a self-complementary recognition pattern based on diacetylene-linked alternating hexylbenzene and perfluorobenzene rings. *Chem. Commun.* **2006**, *4134*, 4134. (b) Wang, Q.; Zhong, Y.; Miller, D. P.; Lu, X.; Tang, Q.; Lu, Z.-L.; Zurek, E.; Liu, R.; Gong, B. Self-assembly and molecular recognition in water: tubular stacking and guest-templated discrete assembly of water-soluble, shape-persistent macrocycles. *J. Am. Chem. Soc.* **2020**, *142*, 2915. (c) Wu, X.; Liu, R.; Sathyamoorthy, B.; Yamato, K.; Liang, G.; Shen, L.; Ma, S.; Sukumaran, D. K.; Szyperski, T.; Fang, W.; He, L.; Chen, X.; Gong, B. Discrete stacking of aromatic oligoamide macrocycles. *J. Am. Chem. Soc.* **2015**, *137*, 5879.
(11) (a) Bialas, D.; Zitzler-Kunkel, A.; Kirchner, E.; Schmidt, D.; Würthner, F. Structural and quantum chemical analysis of exciton coupling in homo- and heteroaggregate stacks of merocyanines. *Nat. Commun.* **2016**, *7*, 12949. (b) Kirchner, E.; Bialas, D.; Fennel, F.; Grüne, M.; Würthner, F. Defined merocyanine dye stacks from a dimer up to an octamer by spacer-encoded self-assembly approach. *J. Am. Chem. Soc.* **2019**, *141*, 7428. (c) Talukdar, P.; Bollot, G.; Mareda, J.; Sakai, N.; Matile, S. Synthetic ion channels with rigid-rod π-Stack architecture that open in response to charge-transfer complex formation. *J. Am. Chem. Soc.* **2005**, *127*, 6528.
(12) (a) Nelson, J. C.; Saven, J. G.; Moore, J. S.; Wolynes, P. G. Solvophobically driven folding of nonbiological oligomers. *Science* **1997**, *277*, 1793. (b) Ohkita, M.; Lehn, J.-M.; Baum, G.; Fenske, D. Helicity coding: Programmed molecular self-organization of achiral nonbiological strands into multiturn helical superstructures: synthesis and characterization of alternating pyridine−pyrimidine oligomers. *Chem. − Eur. J.* **1999**, *5*, 3471. (c) Jiang, H.; Léger, J.-M.; Huc, I.

Aromatic δ-peptides. *J. Am. Chem. Soc.* **2003**, *125*, 3448. (d) Dolain, C.; Léger, J.-M.; Delsuc, N.; Gornitzka, H.; Huc, I. Probing helix propensity of monomers within a helical oligomer. *Proc. Natl. Acad. Sci. U. S. A.* **2005**, *102*, 16146. (e) Hu, Z.-Q.; Hu, H.-Y.; Chen, C.-F. Phenanthroline dicarboxamide-based helical foldamers: Stable helical structures in methanol. *J. Org. Chem.* **2006**, *71*, 1131. (f) Hua, Y.; Liu, Y.; Chen, C.-H.; Flood, A. H. Hydrophobic collapse of foldamer capsules drives picomolar-level chloride binding in aqueous acetonitrile solutions. *J. Am. Chem. Soc.* **2013**, *135*, 14401. (g) Mathew, S. M.; Engle, J. T.; Ziegler, C. J.; Hartley, C. S. The role of arene−arene interactions in the folding of *ortho*-phenylenes. *J. Am. Chem. Soc.* **2013**, *135*, 6714. (h) Mathew, S.; Crandall, L. A.; Ziegler, C. J.; Hartley, C. S. Enhanced helical folding of *ortho*-phenylenes through the control of aromatic stacking interactions. *J. Am. Chem. Soc.* **2014**, *136*, 16666. (i) Gong, B. Crescent oligoamides: From acyclic "macrocycles" to folding nanotubes. *Chem. − Eur. J.* **2001**, *7*, 4336. (j) Zhu, J.; Parra, R. D.; Zeng, H.; Skrzypczak-Jankun, E.; Zeng, X. C.; Gong, B. A new class of folding oligomers: Crescent oligoamides. *J. Am. Chem. Soc.* **2000**, *122*, 4219. (k) Gong, B.; Zeng, H. Q.; Zhu, J.; Yua, L. H.; Han, Y. H.; Cheng, S. Z.; Furukawa, M.; Parra, R. D.; Kovalevsky, A. Y.; Mills, J. L.; Skrzypczak-Jankun, E.; Martinovic, S.; Smith, R. D.; Zheng, C.; Szyperski, T.; Zeng, X. C. Creating nanocavities of tunable sizes: Hollow helices. *Proc. Natl. Acad. Sci. U. S. A.* **2002**, *99*, 11583. (l) Yuan, L.; Zeng, H.; Yamato, K.; Sanford, A. R.; Feng, W.; Atreya, H. S.; Sukumaran, D. K.; Szyperski, T.; Gong, B. Helical aromatic oligoamides: Reliable, readily predictable folding from the combination of rigidified structural motifs. *J. Am. Chem. Soc.* **2004**, *126*, 16528.

(13) (a) Lokey, R. S.; Iverson, B. L. Synthetic molecules that fold into a pleated secondary structure in solution. *Nature* **1995**, *375*, 303. (b) Ghosh, S.; Ramakrishnan, S. Aromatic donor−acceptor charge-transfer and metal-ion-complexation-assisted folding of a synthetic polymer. *Angew. Chem., Int. Ed.* **2004**, *43*, 3264. (c) Zhao, X.; Jia, M.-X.; Jiang, X.-K.; Wu, L.-Z.; Li, Z.-T.; Chen, G.-J. Zipper-featured δ-peptide foldamers driven by donor−acceptor interaction: Design, synthesis, and characterization. *J. Org. Chem.* **2004**, *69*, 270. (d) Gabriel, G. J.; Sorey, S.; Iverson, B. L. Altering the folding patterns of naphthyl trimers. *J. Am. Chem. Soc.* **2005**, *127*, 2637. (e) Hu, X.; Lindner, J. O.; Würthner, F. Stepwise folding and self-assembly of a merocyanine folda-pentamer. *J. Am. Chem. Soc.* **2020**, *142*, 3321.

(14) (a) Takai, A.; Yasuda, T.; Ishizuka, T.; Kojima, T.; Takeuchi, M. Directly-linked ferrocene-naphthalenediimide conjugate: Precise control of stacking structures of π-systems upon redox stimuli. *Angew. Chem., Int. Ed.* **2013**, *52*, 9167. (b) Prabhakaran, P.; Puranik, V. G.; Chandran, J. N.; Rajamohanan, P. R.; Hofmann, H.-J.; Sanjayan, G. J. Novel foldamer structural architecture from cofacial aromatic building blocks. *Chem. Commun.* **2009**, *3446*, 3446. (c) Kaufmann, C.; Bialas, D.; Stolte, M.; Würthner, F. Discrete π-stacks of perylene bisimide dyes within folda-dimers: Insight into long- and short-range exciton coupling. *J. Am. Chem. Soc.* **2018**, *140*, 9986. (d) Krebs, F. C.; Jørgensen, M. Synthesis and structural characterization of new stiff rod oligomeric domains by X-ray crystallography and NMR. *J. Org. Chem.* **2002**, *67*, 7511. (e) Nair, R. V.; Kheria, S.; Rayavarapu, S.; Kotmale, A. S.; Jagadeesh, B.; Gonnade, R. G.; Puranik, V. G.; Rajamohanan, P. R.; Sanjayan, G. J. A Synthetic zipper peptide motif orchestrated via co-operative interplay of hydrogen bonding, aromatic stacking, and backbone chirality. *J. Am. Chem. Soc.* **2013**, *135*, 11477. (f) Mrksich, M.; Parks, M. E.; Dervan, P. B. Hairpin Peptide Motif. A new class of oligopeptides for sequence-specific recognition in the minor groove of double-helical DNA. *J. Am. Chem. Soc.* **1994**, *116*, 7983. (g) Atcher, J.; Nagai, A.; Mayer, P.; Maurizot, V.; Tanatani, A.; Huc, I. Aromatic β-sheet foldamers based on tertiary squaramides. *Chem. Commun.* **2019**, *55*, 10392.

(15) (a) Maurizot, V.; Massip, S.; Léger, J.-M.; Déléris, G. Cylindrical sheet formation of oligo-meta-aniline foldamers. *Chem. Commun.* **2009**, *5698*, 5698. (b) Sebaoun, L.; Maurizot, V.; Granier, T.; Kauffmann, B.; Huc, I. Aromatic oligoamide β-sheet foldamers. *J. Am. Chem. Soc.* **2014**, *136*, 2168. (c) Sebaoun, L.; Kauffmann, B.; Delclos, T.; Maurizot, V.; Huc, I. Assessing stabilization through π−π interactions in aromatic oligoamide β-sheet foldamers. *Org. Lett.* **2014**, *16*, 2326. (d) Lamouroux, A.; Sebaoun, L.; Wicher, B.; Kauffmann, B.; Ferrand, Y.; Maurizot, V.; Huc, I. Controlling dipole orientation through curvature: Aromatic foldamer bent β-sheets and helix−sheet−helix architectures. *J. Am. Chem. Soc.* **2017**, *139*, 14668. (e) Gole, B.; Kauffmann, B.; Maurizot, V.; Huc, I.; Ferrand, Y. Light-controlled conformational switch of an aromatic oligoamide foldamer. *Angew. Chem., Int. Ed.* **2019**, *58*, 8063.

(16) (a) Li, X.; Markandeya, N.; Jonusauskas, G.; McClenaghan, N. D.; Maurizot, V.; Denisov, S. A.; Huc, I. Photoinduced electron transfer and hole migration in nanosized helical aromatic oligoamide foldamers. *J. Am. Chem. Soc.* **2016**, *138*, 13568. (b) Carini, M.; Ruiz, M. P.; Usabiaga, I.; Fernandez, J. A.; Cocinero, E. J.; Melle-Franco, M.; Diez-Perez, I.; Mateo-Alonso, A. High conductance values in π-folded molecular junctions. *Nat. Commun.* **2017**, *8*, 15195. (c) Iwane, M.; Tada, T.; Osuga, T.; Murase, T.; Fujita, M.; Nishino, T.; Kigu-chi, M.; Fujii, S. Controlling stacking order and charge transport in π-stacks of aromatic molecules based on surface assembly. *Chem. Commun.* **2018**, *54*, 12443. (d) Wolffs, M.; Delsuc, N.; Veldman, D.; Vân Anh, N.; Williams, R. M.; Meskers, S. C. J.; Janssen, R. A. J.; Huc, I.; Schenning, A. P. H. J. Helical aromatic oligoamide foldamers as organizational scaffolds for photoinduced charge transfer. *J. Am. Chem. Soc.* **2009**, *131*, 4819. (e) Méndez-Ardoy, A.; Markandeya, N.; Li, X.; Tsai, Y.-T.; Pecastaings, G.; Buffeteau, T.; Maurizot, V.; Muccioli, L.; Castet, F.; Huc, I.; Bassani, D. M. Multi-dimensional charge transport in supramolecular helical foldamer assemblies. *Chem. Sci.* **2017**, *8*, 7251. (f) Mateus, P.; Jacquet, A.; Ardoy, A.; Boulloy, A.; Kauffmann, B.; Pecastaings, G.; Buffeteau, T.; Ferrand, Y.; Bassani, D.; Huc, I. Sensing a binding event through charge transport variations using an aromatic oligoamide capsule. *Chem. Sci.* **2021**, *12*, 3743.

(17) (a) Ohta, E.; Sato, H.; Ando, S.; Kosaka, A.; Fukushima, T.; Hashizume, D.; Yamasaki, M.; Hasegawa, K.; Muraoka, A.; Ushiyama, H.; Yamashita, K.; Aida, T. Redox-responsive molecular helices with highly condensed π-clouds. *Nat. Chem.* **2011**, *3*, 68. (b) Lautrette, G.; Aube, C.; Ferrand, Y.; Pipelier, M.; Blot, V.; Thobie, C.; Kauffmann, B.; Dubreuil, D.; Huc, I. Tuning the guest-binding ability of a helically folded capsule by in situ modification of the aromatic oligoamide backbone. *Chem. − Eur. J.* **2014**, *20*, 1547.

(18) (a) Tie, C.; Gallucci, J. C.; Parquette, J. R. Helical conformational dynamics and photoisomerism of alternating pyridine dicarboxamide/m-(phenylazo)azobenzene oligomers. *J. Am. Chem. Soc.* **2006**, *128*, 1162. (b) Yu, Z.; Hecht, S. Reversible and quantitative denaturation of amphiphilic oligo(azobenzene) foldamers. *Angew. Chem., Int. Ed.* **2011**, *50*, 1640. (c) Parks, F. C.; Liu, Y.; Debnath, S.; Stutsman, S. R.; Raghavachari, K.; Flood, A. H. Allosteric control of photofoldamers for selecting between anion regulation and double-to-single helix switching. *J. Am. Chem. Soc.* **2018**, *140*, 17711. (d) Hua, Y.; Flood, A. H. Flipping the switch on chloride concentrations with a light-active foldamer. *J. Am. Chem. Soc.* **2010**, *132*, 12838. (e) Pramanik, S.; Kauffmann, B.; Hecht, S.; Ferrand, Y.; Huc, I. Light-mediated chiroptical switching of an achiral foldamer host in presence of a carbohydrate guest. *Chem. Commun.* **2021**, *57*, 93.

(19) (a) Kim, K. M.; Song, G.; Lee, S.; Jeon, H.; Chae, W.; Jeong, K.-S. Template-directed quantitative one-pot synthesis of homochiral helical receptors enabling enantioselective binding. *Angew. Chem., Int. Ed.* **2020**, *59*, 22475. (b) Masu, H.; Mizutani, I.; Kato, T.; Azumaya, I.; Yamaguchi, K.; Kishikawa, K.; Kohmoto, S. Naphthalene- and anthracene-Based aromatic foldamers with iminodicarbonyl linkers: their stabilities and application to a chiral photochromic system using retro [4 + 4] cycloaddition. *J. Org. Chem.* **2006**, *71*, 8037.

(20) For reviews see: (a) Bouas-Laurent, H.; Castellan, A.; Desvergne, J.-P.; Lapouyade, R. Photodimerization of anthracenes in fluid solution: structural aspects. *Chem. Soc. Rev.* **2000**, *29*, 43. (b) Bouas-Laurent, H.; Castellan, A.; Desvergne, J.-P.; Lapouyade, R. Photodimerization of anthracenes in fluid solutions: (part 2) mechanistic aspects of the photocycloaddition and of the photochemical and thermal cleavage. *Chem. Soc. Rev.* **2001**, *30*, 248.

https://doi.org/10.1021/jacs.2c01269
J. Am. Chem. Soc. 2022, 144, 6894−6906

(21) (a) Bouas-Laurent, H.; Castellan, A.; Daney, M.; Desvergne, J.-P.; Guiband, G.; Marsau, P.; Riffaud, M. H. Cation-directed photochemistry of an anthraceno-crown ether. *J. Am. Chem. Soc.* **1986**, *108*, 315. (b) Huang, Z.-A.; Chen, C.; Yang, X.-D.; Fan, X.-B.; Zhou, W.; Tung, C.-H.; Wu, L.-Z.; Cong, H. Synthesis of oligoparaphenylene-derived nanohoops employing an anthracene photodimerization−cycloreversion strategy. *J. Am. Chem. Soc.* **2016**, *138*, 11144.

(22) (a) Tanabe, J.; Taura, D.; Ousaka, N.; Yashima, E. Chiral template-directed regio-, diastereo-, and enantioselective photodimerization of an anthracene derivative assisted by complementary amidinium−carboxylate salt bridge formation. *J. Am. Chem. Soc.* **2017**, *139*, 7388. (b) Kissel, P.; Murray, D. J.; Wulftange, W. J.; Catalano, V. J.; King, B. T. A nanoporous two-dimensional polymer by single-crystal-to-single-crystal photopolymerization. *Nat. Chem.* **2014**, *6*, 774. (c) Kawanami, Y.; Katsumata, S. Y.; Nishijima, M.; Fukuhara, G.; Asano, K.; Suzuki, T.; Yang, C.; Nakamura, A.; Mori, T.; Inoue, Y. Supramolecular photochirogenesis with a higher-order complex: highly accelerated exclusively head-to-head Photo-cyclodimerization of 2-Anthracenecarboxylic acid via 2:2 complexation with prolinol. *J. Am. Chem. Soc.* **2016**, *138*, 12187. (d) Kory, M. J.; Worle, M.; Weber, T.; Payamyar, P.; van de Poll, S. W.; Dshemuchadse, J.; Trapp, N.; Schluter, A. D. Gram-scale synthesis of two-dimensional polymer crystals and their structure analysis by X-ray diffraction. *Nat. Chem.* **2014**, *6*, 779. (e) Nakamura, A.; Inoue, Y. Supramolecular Catalysis of the Enantiodifferentiating [4 + 4] Photocyclodimerization of 2-Anthracenecarboxylate by γ-Cyclodextrin. *J. Am. Chem. Soc.* **2003**, *125*, 966. (f) Yao, J.; Yan, Z.; Ji, J.; Wu, W.; Yang, C.; Nishijima, M.; Fukuhara, G.; Mori, T.; Inoue, Y. Ammonia-driven chirality inversion and enhancement in enantiodifferentiating photocyclodimerization of 2-anthracene carboxylate mediated by diguanidino-γ-cyclodextrin. *J. Am. Chem. Soc.* **2014**, *136*, 6916. (g) Bhola, R.; Payamyar, P.; Murray, D. J.; Kumar, B.; Teator, A. J.; Schmidt, M. U.; Hammer, S. M.; Saha, A.; Sakamoto, J.; Dieter Schlüter, A.; King, B. T. A two-dimensional polymer from the anthracene dimer and triptycene motifs. *J. Am. Chem. Soc.* **2013**, *135*, 14134.

(23) (a) Ihmels, H.; Mohrschladt, C. J.; Schmitt, A.; Bressanini, M.; Leusser, D.; Stalke, D. Highly regioselective solid-state photodimerization of naphthoquinolizinium salts. *Eur. J. Org. Chem.* **2002**, *2002*, 2624. (b) Jouvenot, D.; Glazer, E. C.; Tor, Y. Photodimerizable ditopic ligand. *Org. Lett.* **1987**, *2006*, 8. (c) Berni, E.; Dolain, C.; Kauffmann, B.; Léger, J.-M.; Zhan, C.; Huc, I. Expanding the registry of aromatic amide foldamers: Folding, photochemistry and assembly using diaza-anthracene units. *J. Org. Chem.* **2008**, *73*, 2687. (d) Li, M.; Schluter, A. D.; Sakamoto, J. Solid-state photopolymerization of a shape-persistent macrocycle with two 1,8-diazaanthracene units in a single crystal. *J. Am. Chem. Soc.* **2012**, *134*, 11721. (e) Payamyar, P.; Servalli, M.; Hungerland, T.; Schutz, A. P.; Zheng, Z.; Borgschulte, A.; Schluter, A. D. Approaching two-dimensional copolymers: Photoirradiation of anthracene- and diaza-anthracene-bearing monomers in Langmuir monolayers. *Macromol. Rapid Commun.* **2015**, *36*, 151. (f) Lunchev, A. V.; Morris, S. A.; Ganguly, R.; Grimsdale, A. C. Synthesis and electronic properties of novel 5,7-diazapentacene derivatives. *Chem. − Eur. J.* **1819**, *2019*, 25.

(24) Only negligible amounts of photoproducts were detectable by ^{1}H NMR. Spectrophotometric investigations allowed for the measurement of a quantum yield about two orders of magnitude lower than for other compounds (Table 1). The observation that the photoproduct does not accumulate suggests that it is thermally unstable, contrary to the head-to-tail photodimer of A^{Me}.

(25) The pyridine photoproducts can be excited at shorter wavelengths. At these wavelengths, all other aromatic moieties of the oligomers also absorb, making the fraction of light available to the photodimer to regenerate the starting material extremely small. This is compounded by the possibility of electronic energy transfer from the excited photodimer to the neighboring aromatic units, effectively de-exciting the photodimer and impeding the photoreversion.

(26) Kendhale, A. M.; Poniman, L.; Dong, Z.; Laxmi-Reddy, K.; Kauffmann, B.; Ferrand, Y.; Huc, I. Absolute control of helical handedness in quinoline oligoamides. *J. Org. Chem.* **2011**, *76*, 195.

(27) Miwa, K.; Furusho, Y.; Yashima, E. Ion-triggered spring-like motion of a double helicate accompanied by anisotropic twisting. *Nat. Chem.* **2010**, *2*, 444.

https://doi.org/10.1021/jacs.2c01269
J. Am. Chem. Soc. 2022, 144, 6894−6906